ROYAL SOCIETY OF CHEMISTRY

EDGE ARTICLE

Check for updates

Acid-responsive singlet oxygen nanodepots†

Zengwei Ran,‡[a] Maolin Wang,‡[a] Zhu Yuan,[b] Yan Zhang,*[b] Guhuan Liu [iD] *[a] and Ronghua Yang [iD] *[a]

The singlet oxygen carrier addresses the challenges of traditional photodynamic therapy (PDT), which relies on the presence of oxygen within solid tumors and struggles with light penetration issues. However, the inability to control the release of singlet oxygen has hindered precise treatment applications. Here, we introduce an acid-responsive singlet oxygen nanodepot (aSOND) designed to overcome this limitation. The aSOND is synthesized using a responsive diblock copolymer system that includes a hydrophilic PEG block and a pH-responsive block with singlet oxygen loading sites. In neutral or alkaline environments, the aSOND releases singlet oxygen slowly, ensuring stability in blood circulation. In contrast, in acidic environments such as the tumor microenvironment or intracellular lysosomes, protonation of the tertiary amine group within the pH responsive block increases the hydration of the polymer, triggering a rapid release of singlet oxygen. This feature enables controlled, tumor-specific release of reactive oxygen species (ROS). The aSOND system effectively implements an "OFF−ON" singlet oxygen therapy, demonstrating high spatiotemporal selectivity and independence from both oxygen supply and external light, offering a promising approach for targeted cancer therapy.

Introduction

Photodynamic therapy (PDT) is a non-invasive and effective cancer treatment strategy that utilizes photosensitizers (PSs) to generate reactive oxygen species (ROS), specifically singlet oxygen ($^1O_2$), to induce cancer cell death.[1–6] However, the therapeutic efficacy of PDT is significantly limited by the hypoxic nature of the tumor microenvironment, where oxygen concentrations typically range from 0% to 2%.[7–9] This hypoxia impairs the oxygen-dependent mechanisms of conventional PDT, reducing its effectiveness. Additionally, PDT is constrained by the limited depth of light penetration into tissues, as the visible or near-infrared (NIR) light commonly used can only penetrate 0.5–2 mm into the skin or tumor tissue.[10] This limitation is particularly problematic for treating larger tumors or internal malignancies, such as lung metastases. To overcome these challenges, researchers are exploring alternative approaches for ROS generation that do not rely solely on oxygen and allow for deeper tissue penetration, such as sonodynamic therapy (SDT)

and X-ray-induced photodynamic therapy (X-PDT).[11–13] These methods offer promising strategies to enhance the therapeutic reach and effectiveness of ROS-based cancer treatments.

A novel approach to address both the hypoxic tumor environment and the limitations of light penetration is the development of singlet oxygen depot (SOD) systems.[14–19] These systems are designed to store $^1O_2$ generated *in vitro* and release it *in vivo*, enabling oxygen- and light-independent ROS therapies. For instance, Zou *et al.* reported a diblock copolymer based on 2-pyridone that facilitates $^1O_2$-based therapy,[18] while Xie *et al.* introduced a metal–organic framework-based poly-pyridone system for the delivery of singlet oxygen.[15] In these systems, the pyridone moiety is pivotal during both the storage and release phases, facilitating a sustained release of $^1O_2$. Furthermore, singlet oxygen depots are classified as gaso-transmitters, akin to the endogenously produced gases including nitric oxide (NO), carbon monoxide (CO), and hydrogen sulfide (H_2S). These gasotransmitters have demonstrated substantial therapeutic potential in addressing a spectrum of severe pathologies, such as cardiovascular disorders, inflammatory conditions, bacterial infections, and oncological diseases.[20–24]

Ideally, a SOD system would demonstrate an "ON–OFF" release mechanism, where $^1O_2$ is securely stored during circulation in the bloodstream, thus minimizing side effects and avoiding premature release, and then it is promptly released upon reaching the tumor microenvironment. Recent developments include the work by Akkaya *et al.*, who demonstrated that elevated temperatures could enhance the release of $^1O_2$, with the release being triggered by photo-thermal effects.[16]

[a]*Key Laboratory of Chemical Biology & Traditional Chinese Medicine Research, Ministry of Education, Institute of Interdisciplinary Studies, College of Chemistry and Chemical Engineering, Hunan Normal University, Changsha, Hunan 410081, China. E-mail: ghliu@hunnu.edu.cn; yangrh@pku.edu.cn*

[b]*National & Local Joint Engineering Laboratory for New Petro-chemical Materials and Fine Utilization of Resources, Key Laboratory of Light Energy Conversion Materials of Hunan Province College, College of Chemistry and Chemical Engineering, Hunan Normal University, Changsha, Hunan 410081, China. E-mail: zyzsxd@163.com*

† Electronic supplementary information (ESI) available. See DOI: https://doi.org/10.1039/d4sc06553k

‡ These authors contributed equally.

Additionally, Akkaya *et al.* documented the production of $^1O_2$ initiated by the activation of nitroreductase.[14] Liu *et al.* recently developed a pyridone–pyridine transition system that is responsive to ROS, enabling the controlled release of $^1O_2$.[25]

Herein, we report an acid-responsive singlet oxygen nanodepot (aSOND). The aSOND was synthesized using a reactive diblock copolymer system comprising a hydrophilic polyethylene glycol (PEG) block and a pH-responsive block. The pH-responsive segment is formed by the copolymerization of *N,N*-diethylaminoethyl methacrylate (DEAEMA), which imparts pH sensitivity, and 1-(4-vinylbenzyl)pyridin-2(1*H*)-one (VBP), which provides sites for $^1O_2$ loading. $^1O_2$, generated through methylene blue under light irradiation, was encapsulated within these block copolymers, which subsequently self-assembled into nanomicelles under aqueous conditions, creating aSONDs. In neutral or alkaline environments, the release of $^1O_2$ from the aSOND is slow, maintaining stability during circulation. However, in acidic environments, such as the tumor microenvironment or intracellular lysosomes, the protonation of the DEAEMA tertiary amine groups increases the hydration of the polymer, triggering a rapid release of $^1O_2$. This enables controlled, tumor-specific release of $^1O_2$. The aSOND system effectively achieves an "OFF–ON" $^1O_2$ therapy, exhibiting high spatiotemporal selectivity, while being independent of both oxygen supply and external light illumination.

Results and discussion

Preparation of aSONDs

The synthesis of aSONDs involves a tripartite process: the creation of block copolymers, the incorporation of $^1O_2$, and the self-assembly into nanostructures (Fig. 1A). The monomer 1-(4-vinylbenzyl)pyridin-2(1*H*)-one (VBP), which supports singlet oxygen, was synthesized and verified through ^1H and ^{13}H NMR (Fig. S1†). Utilizing the polyethylene glycol macromolecular chain transfer agent, we executed reversible addition–fragmentation chain transfer (RAFT) copolymerization of *N,N*-diethylaminoethyl methacrylate (DEAEMA) with VBP to fabricate diblock copolymers. Four distinct block copolymers, designated as **P1–P4**, were synthesized, each varying in VBP

Fig. 1 Schematic illustration of the operation of the acid-responsive singlet oxygen nanodepot (aSOND).

content; notably, **P1** lacks the DMAEMA unit, rendering it non-responsive to pH changes. These copolymers were structurally characterized using ^1H NMR and gel permeation chromatography (GPC, Fig. S2†), with their detailed chemical structures outlined in Table S1.†

Subsequent loading of singlet oxygen was achieved by illuminating methylene blue, facilitating the conversion of oxygen to singlet oxygen, which was then absorbed by the block copolymers, forming singlet oxygen-loaded polymers **OP1–OP4**. According to ^1H NMR analysis, approximately 60% of the pyridone groups were loaded with singlet oxygen (Fig. S3†). These loaded copolymers were then directly introduced into water without prior purification, leading to their self-assembly into aSONDs. Characterization of the resulting nanostructures *via* transmission electron microscopy (TEM) and dynamic light scattering (DLS) revealed an average diameter of ~150 nm for the aSONDs (Fig. 1B).

pH regulated $^1O_2$ release

We subsequently investigated the pH responsiveness of the aSOND, using **OP3** as a model system. When the freshly prepared aSOND was dispersed in an acidic medium (pH 5.0), both TEM and DLS analyses showed a slight increase in particle diameter, accompanied by a broader distribution of hydrodynamic size. This observation suggests that protonation of the tertiary amine groups in the micelle core led to swelling, although the hydrophobic nature of VBP prevented micellar collapse. After incubating the aSOND for 24 hours under both neutral (pH 7.4) and acidic (pH 5) conditions, during which all singlet oxygen was released, a notable increase in micelle diameter was observed at both pH levels. This increase can be attributed to the enhanced hydrophilicity of the micellar core following singlet oxygen release.

We further monitored the release kinetics of singlet oxygen from the aSOND at pH 5 and pH 7.4 using 2,7-dichlorodihydrofluorescein diacetate (DCFH) as a reporter. DCFH is oxidized by $^1O_2$ to produce highly fluorescent DCF, allowing us to track singlet oxygen release. The results clearly demonstrated that the aSOND released singlet oxygen more rapidly at pH 5 compared to pH 7.4. Among the polymers tested, **OP4**, which contains a higher proportion of DEAEMA, showed the fastest release, suggesting that the hydration of the micelle core is the primary factor driving the accelerated ROS release (Fig. 2E). In contrast, **OP1**, which lacks DEAEMA, did not exhibit pH-responsive singlet oxygen release (Fig. 2F). However, when **OP1** and **OP3** were dissolved in a DMSO/H$_2$O (8/2) mixture, rapid singlet oxygen release occurred due to complete hydration, and no pH-regulated release behavior was observed (Fig. 2G). Following the release of singlet oxygen, there was a gradual reduction in the DLS light scattering intensity of the nanomicelles, likely resulting from the loosening of the nanomicelles' packing after the oxygen was released (Fig. 2H).

To further investigate the core hydration under acidic conditions, Nile red, a polarity-sensitive fluorescent probe, was encapsulated within the micelles. Nile red fluorescence diminishes in highly polar environments, making it a useful indicator of core hydration. When the pH of the system was adjusted, **OP3**
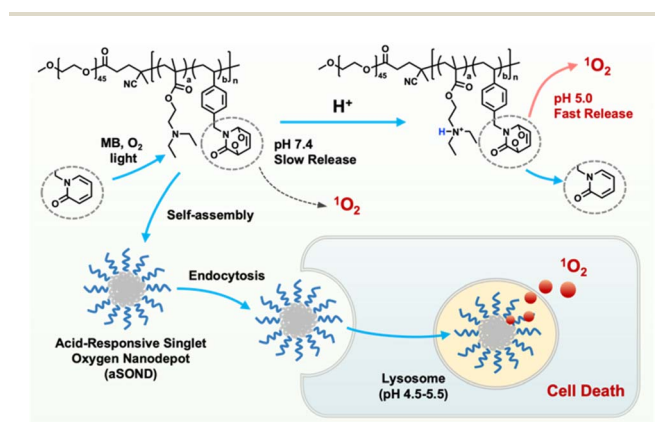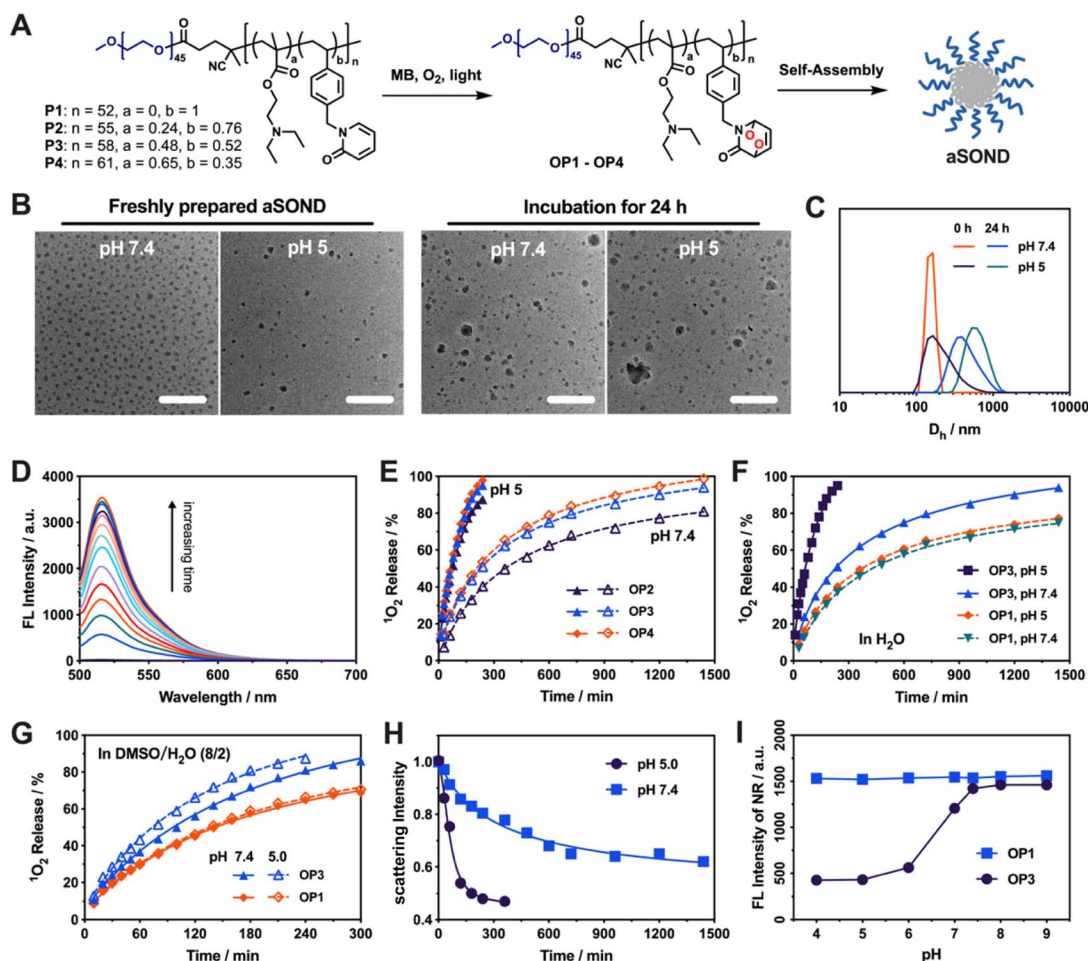
Fig. 2 (A) Schematic illustration of the preparation process for the acid-responsive singlet oxygen nanodepot (aSOND). (B) Representative TEM images of the aSOND prepared from **OP3**, showing a freshly prepared aSOND (left) and the aSOND after 24 hours of incubation at pH 5.0 and pH 7.4 (right). Scale bar: 2 μm. (C) Hydrodynamic diameter distribution measured by dynamic light scattering (DLS) under the same conditions as in (B). (D–G) Assessment of $^1O_2$ release from the aSOND under various conditions using 2,7-dichlorodihydrofluorescein diacetate (DCFH). (D) Typical fluorescence change of DCFH. (E and F) Singlet oxygen release profiles at pH 5.0 and pH 7.4 of the aSOND prepared using **OP1–OP4**. (G) Singlet oxygen release profiles of **OP1** and **OP3** fully dissolved in DMSO/H$_2$O (8/2). (H) Time-dependent DLS scattering intensities recorded for the **OP3** aSOND at pH 7.4 and 5.0. (I) Fluorescence emission of Nile red loaded in the aSOND as a function of pH.

showed a significant decrease in Nile red fluorescence under acidic conditions, while **OP1** exhibited little change (Fig. 2H). Based on these findings, we propose that protonation of the micellar core in acidic environments promotes core hydration, thereby facilitating water access to the singlet oxygen-loaded pyridinium moieties and resulting in rapid singlet oxygen release (Fig. 2I).

Intracellular acidity triggered $^1O_2$ release

The acid-induced singlet oxygen release capability of aSONDs facilitates their prompt and site-specific liberation in the acidic milieu of tumor cells. We proceeded to explore the acid-selective emancipation of aSONDs in cellular environments. For this purpose, **OP5**, labeled with the fluorophore rhodamine B (RhB), was synthesized to track the cellular entry of aSONDs (Fig. 3A). CLSM analysis revealed that the **OP5**-based aSOND was rapidly endocytosed, with prominent red RhB fluorescence manifesting within 1 h of co-culture with HepG2 cells (Fig. 3B). Moreover,

there was significant colocalization with LysoTracker, a lyso-somal marker, suggesting that the aSOND was internalized into the acidic lysosomes following endocytosis (Fig. 3C).

Upon entry into lysosomes, the acidic conditions therein facilitate the production of singlet oxygen by the aSOND. We employed DCFH, which upon oxidation by ROS generates strongly fluorescent DCF, to monitor intracellular singlet oxygen levels. Both CLSM and flow cytometry analyses indicated that the aSOND based on **OP2–OP4** produced substantial singlet oxygen within the cells, resulting in intense green fluorescence. In contrast, **OP1**, lacking acid-triggered ROS release capabilities, did not facilitate rapid singlet oxygen release, leading to faint green fluorescence in cells. Among **OP2–OP4**, **OP3** exhibited the highest singlet oxygen production capacity, attributed to **OP2** having fewer acid-responsive groups and **OP4** having a limited loading capacity for singlet oxygen (Fig. 3D–F).

To underscore the influence of cellular acidity on ROS release, we manipulated the acid–base balance within cells
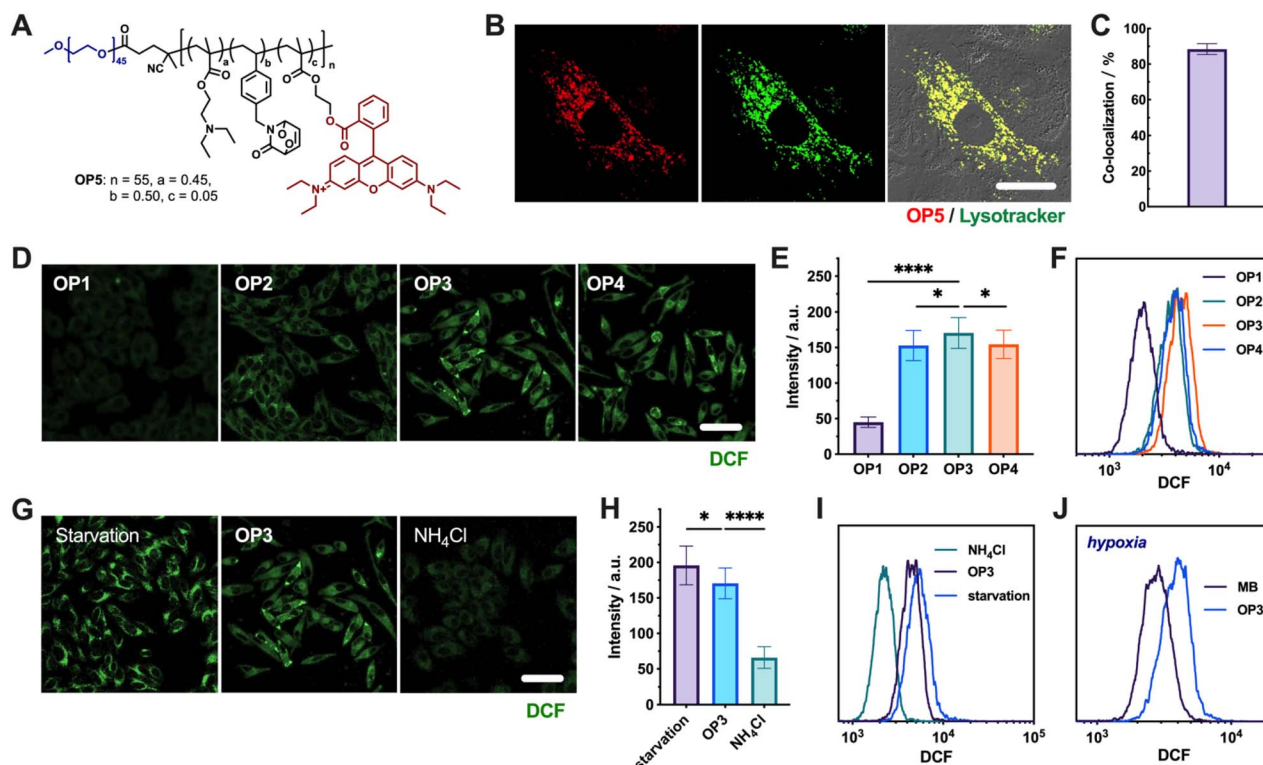
Fig. 3 (A) The chemical structure of a rhodamine B-labeled block copolymer (OP5) designed for intracellular imaging of aSONDs. (B and C) CLSM images of an OP5-based aSOND (0.1 g L^{-1}) incubated with HepG2 cells for 1 h (B), and the colocalization ratio of OP5 fluorescence with LysoTracker (C). Lysosomes were pre-labeled using LysoTracker Green. Green and red channel emissions were collected at 540 $\pm$ 20 nm and 630 $\pm$ 20 nm, respectively. Scale bar: 5 μm. (D–F) CLSM images of DCFH (1 μM) and OP1–OP4 (0.2 g L^{-1}) co-cultured with HepG2 cells for 2 h (D), and green DCF fluorescence intensities (t-test; ****$p < 0.0001$ and *$p < 0.05$) from CLSM images (E), and from flow cytometry analysis (F). Scale bar: 20 μm. (G–I) CLSM images (G) and DCF intensities (t-test; ****$p < 0.0001$ and *$p < 0.05$) from CLSM images (H), and from flow cytometry analysis (I) for DCFH (1 μM) and OP3 (0.2 g L^{-1}) co-cultured with HepG2 cells pretreated under pH-adjusted conditions through starvation and NH$_4$Cl addition. Scale bar: 20 μm. (J) A flow cytometry comparison of the singlet oxygen generation capacity between the OP3-based aSOND and MB-based photodynamic therapy under hypoxic conditions, using DCFH to detect reactive oxygen species. (D and G) Green channel emission was collected at 530 $\pm$ 20 nm. (C, E and H) Error bars represent mean $\pm$ SD from 10 individual cells.

through starvation, which leads to the accumulation of acidic substances intracellularly,[26] and by the addition of NH$_4$Cl, which induces intracellular alkalinization.[27,28] Pre-adjusting the cellular pH followed by incubation with the OP3 aSOND demonstrated that singlet oxygen release was enhanced under starvation-induced acidic conditions, whereas alkaline conditions suppressed ROS release (Fig. 3G–I). This is particularly relevant in rapidly growing tumor cells, which are often nutrient-deficient and thus inherently acidic, favoring the selective release of ROS by the aSOND.

Lastly, we compared the intracellular singlet oxygen generation capabilities of aSONDs and traditional photodynamic therapy (PDT) under hypoxic conditions using flow cytometry. The results showed that the aSOND maintained consistent singlet oxygen production under both normoxic and hypoxic conditions. In contrast, methylene blue (MB)-based PDT exhibited significantly reduced singlet oxygen generation under hypoxic conditions due to its dependence on ambient oxygen (Fig. 3J). These findings highlight that aSONDs can surmount the limitations faced by conventional PDT in the oxygen-deficient tumor microenvironment, offering a promising alternative for effective cancer treatment.

Cell viability and combination with chemotherapy

The cytotoxic effects of OP2–OP4 and P2–P4 on HepG2 cells were evaluated using an MTT assay. As illustrated in Fig. 4A, P2–P4 exhibited no cytotoxicity at concentrations up to 0.3 g L^{-1}, confirming the biocompatibility of the vector. Conversely, OP2–OP4 displayed pronounced cytotoxic effects, with OP3 being the most potent, exhibiting an LC$_{50}$ of 0.071 g L^{-1}, correlating with its superior intracellular singlet oxygen production capacity. Additionally, we observed that cell death initiated ~4 h post-treatment with OP2–OP4, a timeline that aligns with the release kinetics of singlet oxygen under acidic conditions (Fig. S4†). Consistent outcomes were observed in cell viability assays (dead/alive assay), as depicted in Fig. 4B, where OP2–OP4 eradicated approximately 90% of the cells at 0.1 g L^{-1} concentration, while P2–P4 showed negligible cytotoxicity.

Given that aSONDs can rapidly and efficiently release $^1O_2$ within lysosomes, we hypothesized that the primary cause of cytotoxicity was the lysosomal disruptive effect of singlet oxygen. Lysosomes, being critical organelles, play a pivotal role in cellular homeostasis; damage to these organelles can trigger apoptosis.[29–32] To further investigate this, cells treated with OP3
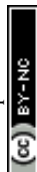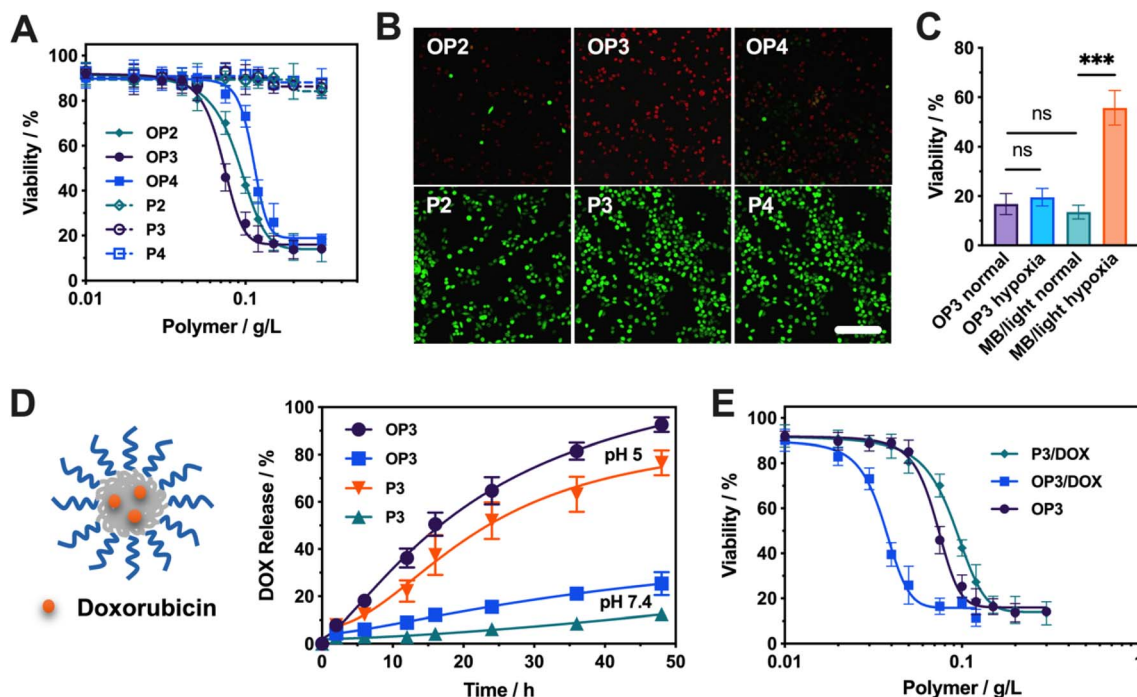
Fig. 4 (A) Dose-dependent cytotoxicity of **OP2–OP4** and **P2–P4** (0.01–0.3 g L^{-1}) to HepG2 cells assessed using MTT assay. (B) Live (green channel)/dead (red channel) assay with HepG2 cells incubated with **OP2–OP4** and **P2–P4** (0.1 g L^{-1}). Green and red channel emissions were recorded at 530 ± 20 nm and 610 ± 20 nm, respectively. Scale bar: 100 μm. (C) Cell viability of **OP3** aSOND (0.1 g L^{-1}) and MB (10 μM) based PDT under normal and hypoxic conditions assessed using MTT assay (t-test; ***$p < 0.001$ and nd > 0.05). (D) Doxorubicin release profile from **P3** and **OP3** (0.1 g L^{-1}) nanoparticles at pH 5 or 7.4. (E) Dose-dependent cytotoxicity of DOX@**OP3**, **OP3**, and DOX@**P3** (0.01–0.3 g L^{-1}) to HepG2 cells assessed using MTT assay.

were stained with LysoTracker to visualize lysosomal damage. Notably, LysoTracker fluorescence diminished significantly after 3 h of treatment and became completely undetectable after 5 h (Fig. S5†). These observations suggest that the aSOND induces lysosomal damage, ultimately leading to cell death.

The cytotoxicity of aSONDs and conventional PDT was also assessed under normoxic and hypoxic conditions. Unlike conventional PDT, aSOND's efficacy was not compromised by varying oxygen levels. At a concentration of 0.1 g L^{-1}, aSONDs maintained high cytotoxicity under both normoxic and hypoxic conditions, with only about 10% of cells surviving. In contrast, MB-based PDT showed high cytotoxicity under normoxic conditions, with less than 10% cell survival, but under hypoxic conditions, its efficacy drastically reduced, leading to a survival rate of 53% (Fig. 4C and S6†). These findings underscore aSOND's capability to effectively eradicate tumor cells under hypoxic conditions.

Responsive amphiphilic polymers, such as those used in aSONDs, have potential applications in chemotherapeutic agent delivery, releasing drugs in response to specific stimuli. We explored combining ROS treatment with chemotherapy by incorporating the chemotherapeutic drug doxorubicin (DOX) into aSONDs. DOX was integrated during the self-assembly process of the block copolymer, leveraging hydrophobic interactions for incorporation into the nanoparticles, with a typical loading efficiency of 8.5%. The pH-responsive nature of the aSOND facilitated rapid DOX release under acidic conditions,

with 94% of the loaded DOX released from the **OP3** aSOND at pH 5 over 48 h. The release from **P3** nanomicelles was slower due to their higher hydrophobicity and denser packing. In contrast, DOX release from both polymeric micelles was slower at pH 7.4, with less than 20% released after 48 h (Fig. 4D). Importantly, DOX remained stable in the presence of $^1O_2$, with 90% of DOX remaining intact when DOX and **OP3** were co-incubated for 48 h (Fig. S7†). This suggests that a combination of chemotherapy using DOX and $^1O_2$ treatment could be effectively utilized.

This drug-loaded aSOND not only rapidly produces singlet oxygen under acidic conditions but also efficiently releases the encapsulated drug, offering a synergistic therapeutic effect. The cytotoxicity of this combined treatment was evaluated, revealing that the DOX-loaded **OP3** aSOND exhibited the highest cyto-toxicity, with an LC_{50} as low as 0.035 g L^{-1} (Fig. 4E). The efficacy of this synergistic approach is further augmented by the lyso-somal disruption caused by the released singlet oxygen, which facilitates the escape of chemotherapeutic agents from the lysosomes—a mechanism analogous to photochemical inter-nalization (PCI).[33–35]

In vivo therapy efficacy

The acid-responsive characteristics of the aSOND facilitate the rapid release of $^1O_2$ within the acidic tumor microenvironment, while its nano-sized architecture allows for tumor enrichment via the Enhanced Permeability and Retention (EPR) effect.[36,37]

Building on these properties, we aimed to evaluate aSOND's $^1O_2$ generation and therapeutic efficacy in a tumor model. The 3D cell spheroid model serves as an *in vitro* approximation of the tumor milieu, providing a relevant platform for initial assessments. Following a 12-hour incubation of the cell spheroids with the **OP3** aSOND under normoxic conditions, and employing Singlet Oxygen Sensor Green (SOSG) for $^1O_2$ detection, we observed widespread green fluorescence, indicative of $^1O_2$ production throughout the entire spheroid. Notably, the core regions of the spheroid exhibited robust green fluorescence, reaching approximately half the intensity observed at the periphery. This finding underscores aSOND's capacity to penetrate the cell sphere and access its interior, owing to its diminutive size. Furthermore, the aSOND demonstrated resilience to hypoxic conditions; the internal hypoxic environment of the spheroid did not impede $^1O_2$ delivery (Fig. 5A and B).

In contrast, under normoxic culture conditions, photodynamic treatment using MB generated substantial $^1O_2$ solely at the periphery of the cell sphere, failing to penetrate the central regions due to hypoxia. Conversely, the aSOND maintained its efficacy, ensuring $^1O_2$ delivery to the spheroid's interior, irrespective of whether the spheroid was cultured under normoxic or hypoxic conditions. This consistency highlights aSOND's unique ability to overcome the limitations imposed by hypoxia, a common challenge in conventional photodynamic therapies (Fig. 5A and B).

Subsequently, we explored the *in vivo* capacity of the aSOND to deliver $^1O_2$ in tumor-bearing mice, where SOSG was injected to quantify $^1O_2$ levels. Upon administration of the **OP3** aSOND *via* the tail artery, we observed a continuous increase in fluorescence within the tumor (Fig. 5C), indicative of aSOND's enrichment at the tumor site *via* the EPR effect. This enrichment facilitated the release of singlet oxygen in response to the acidic environment of the tumor or within acidified tumor cell organelles. The fluorescence intensity within the tumor peaked at approximately 2.5 h, closely matching the release time of the aSOND under acidic conditions (Fig. 5D).

Additionally, we assessed the pharmacokinetic studies of aSONDs. Following tail vein injection, the aSOND demonstrated a half-life of ~45 min in the bloodstream. By 4 h post-injection, the blood concentration had decreased to less than 20% (Fig. S8†). These findings suggest that aSONDs are effectively released in the acidic microenvironment of the tumor site. Furthermore, their rapid metabolism minimizes the potential for significant side effects in other normal tissues, thereby enhancing the therapeutic index and overall safety profile of the treatment.

Subsequently, we evaluated the combined treatment of acid-activated $^1O_2$ and chemotherapy *in vivo* using a murine model with subcutaneous tumors. HepG2 tumor-bearing mice (three mice per group) served as the animal model for this *in vivo* study. To elucidate the anti-tumor efficacy of the aSOND and loaded DOX form *in vivo*, we continuously monitored tumor
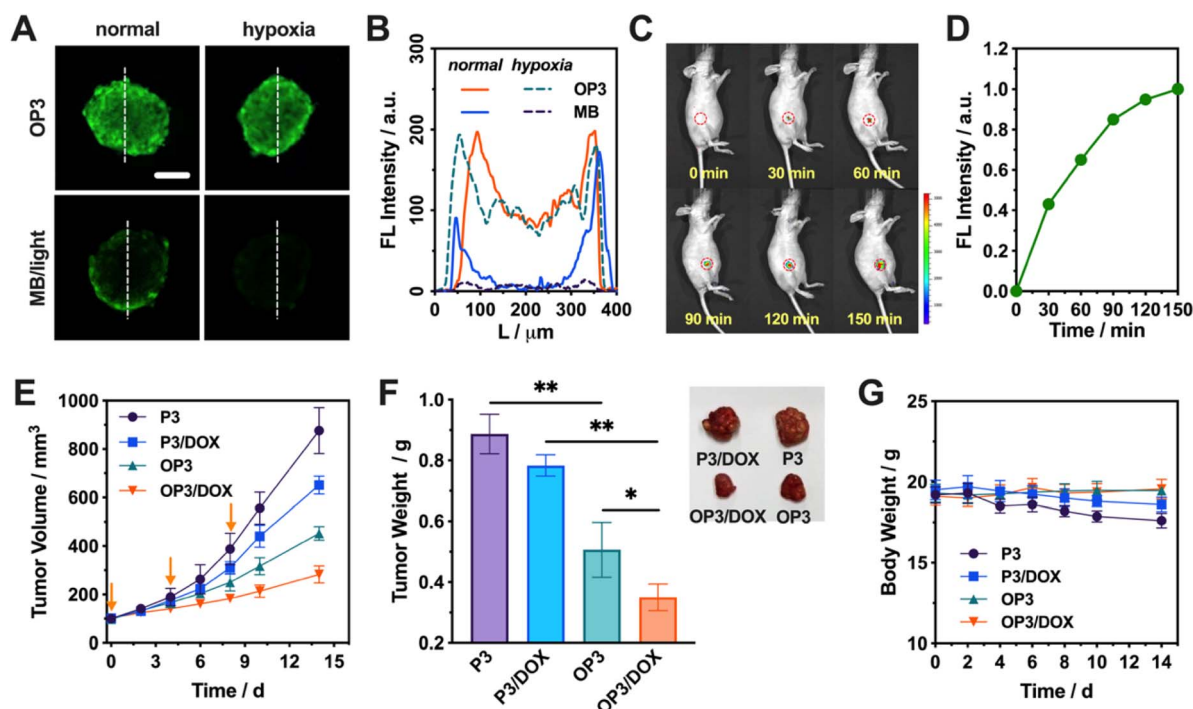

Fig. 5 (A) Representative CLSM images and (B) emission intensity profiles of 3D HepG2 spheroids following treatment with the **OP3**-based aSOND and MB-based photodynamic therapy (PDT) under hypoxic or normoxic conditions, utilizing Singlet Oxygen Sensor Green (SOSG) for $^1O_2$ detection. Green channel emissions were recorded at 530 ± 20 nm. Scale bar: 100 μm. (C) *In vivo* imaging and (D) SOSG emission intensity in HepG2 tumor-bearing mice after coadministration of the **OP3**-based aSOND at varying time points. White circles denote tumor locations. (E) Relative tumor growth curves of mice over a 14-day treatment period (arrows indicate the 3 injection points); (F) on day 14, photographs and tumor volumes of *ex vivo* tumor tissues from mice (*t*-test; **$p < 0.01$ and *$p < 0.05$); (G) body weight change curves of tumor-bearing mice treated with **P3** or **OP3**, with or without DOX. Error bars represent mean $\pm$ SD from 3 parallel experiments.

volume and mouse body over a 14-day period following treatment. Four groups of mice received distinct intravenous formulations: **P3**, **DOX@P3**, **OP3**, and **DOX@OP3**. Initially, tumors were allowed to grow to approximately 100 mm^3, after which mice were administered one of the four treatment formulations.

As depicted in Fig. 5E–G, mice injected with **P3** exhibited a progressive increase in tumor size and weight over the 14-day period, indicating the relatively low cytotoxicity of the **P3** vector. Mice injected with **DOX@OP3** showed only a minimal increase in tumor size and weight, highlighting the maximal inhibition of tumor growth achieved through the combination of $^1O_2$ and chemotherapy. Regarding mouse body weight, a slight decrease was observed in the **P3**-treated group, whereas the body weight of mice receiving effective treatments remained essentially unchanged. These findings indicate that the aSOND, particularly when loaded with DOX, effectively inhibits tumor growth *in vivo* without exacerbating side effects.

Experimental

Preparation of aSONDs

The experimental protocol was conducted as follows: **P1–P4** (10 mg) were dissolved in DMSO (1 mL) and subsequently cooled to 0 °C. Methylene blue (1 μmol) was introduced into the mixture, followed by oxygen bubbling. Irradiation with red light (630 nm) was applied for a duration of 2 h. ^{1}H NMR analysis revealed that, by this stage, 51–62% of the pyridone had been successfully loaded with $^1O_2$ (Fig. S3 and Table S2†). This solution was then swiftly added to deionized water, resulting in the formation of aSONDs.

Cellular uptake and $^1O_2$ detection

The hepatocellular carcinoma cell line HepG2 was obtained from ATCC. HepG2 cells ($\sim 10^5$) in DMEM complete medium were plated onto 35 mm uncoated, glass-bottomed culture dishes and incubated overnight. HepG2 cells were incubated with 2,7-dichlorodihydrofluorescein diacetate (DCFH, 10 μmol) for 1 h, and cells were washed with PBS (3 mL). Then, **OP1–OP4** aSONDs were co-incubated with the cells for an additional 2 h. Fluorescence images were recorded on a confocal laser scanning microscope (CLSM). The samples incubated with DCFH were excited with a 488 nm laser and fluorescence was recorded from 500 to 600 nm. To adjust intracellular pH, an aqueous NH$_4$Cl (30 mM NH$_4$Cl and 30 mM NaCl) and PBS were used, respectively.

In vitro cytotoxicity assay

HepG2 cells were employed for *in vitro* cytotoxicity evaluation *via* the MTT assay. HepG2 cells were seeded in a 96 well plate at an initial density of *ca.* 5000 cells per well in 100 μL of complete DMEM medium. After incubating for 24 h, DMEM was replaced with fresh medium, and the cells were treated with polymer solution at varying final concentrations. The treated cells were incubated for 24 h. 20 μL of MTT reagent (5.0 g L^{-1}, in PBS) was added to each well. The cells were further incubated for 4 h at 37 °C. The medium in each well was then removed and replaced with 150 μL of DMSO. The plate was gently agitated for 15 min before the absorbance at 570 nm was recorded using a microplate reader (Thermo Fisher).

In vivo image and therapy

All animal procedures were performed in accordance with the Guidelines for Care and Use of Laboratory Animals of Hunan Normal University and approved by the Animal Ethics Committee of Hunan Normal University (No. 2023-183). Mice were procured from Hunan People's Hospital and maintained in a standard specific pathogen-free (SPF) environment. HepG2 cells were cultured, harvested, and washed multiple times with PBS to obtain a cell suspension, which was then subcutaneously injected into the right flank of the mice at a concentration of 1×10^6 cells per mouse. Once the tumor volume reached 100 mm^3, the mice were stratified into groups according to the experimental design and treated with the respective drugs *via* intravenous injection at a dose of 5 mg kg^{-1}. For imaging purposes, mice were administered a tail vein injection of the drug (100 μL, 5 mg kg^{-1}). Fluorescence imaging of the mouse aortas was performed using an IVIS® Lumina III *in vivo* imaging system.

Conclusions

We have successfully developed an acid-responsive singlet oxygen nanodepot (aSOND) that addresses key limitations of traditional PDT in oxygen-deficient and poorly illuminated tumor environments. The aSOND, synthesized from a diblock copolymer system featuring a hydrophilic PEG segment and a pH-responsive block, leverages the copolymerization of DEAEMA for pH sensitivity and VBP for $^1O_2$ loading. The system encapsulates $^1O_2$ generated *via* methylene blue under light exposure and forms nanomicelles in aqueous environments, establishing the acid-responsive nanodepots. These aSONDs exhibit slow release of $^1O_2$ under neutral or alkaline conditions, ensuring stability in systemic circulation. In contrast, the acidic conditions prevalent in tumor microenvironments or intracellular lysosomes induce the protonation of DEAEMA, which increases polymer hydration and triggers rapid singlet oxygen release. This mechanism enables controlled, tumor-specific reactive oxygen species (ROS) delivery. Consequently, the aSOND system achieves an "OFF–ON" therapeutic modality, providing high spatiotemporal selectivity and operating independently of external oxygen and light sources, marking a significant advancement in the field of targeted cancer therapy.

Data availability

All data associated with this study are available in the article and ESI.†

Author contributions

All authors have given approval to the final version of the manuscript. Z. R.: conceptualisation, methodology, formal

analysis, writing – original draft, visualisation. M. W.: conceptualisation, methodology, formal analysis. Z. Y.: methodology, formal analysis. Y. Z.: supervision, writing – review & editing, funding acquisition. G. L.: supervision, conceptualisation, writing – review & editing, funding acquisition. R. Y.: supervision, methodology, funding acquisition.

Conflicts of interest

There are no conflicts to declare.

Acknowledgements

Notes and references

1 X. Zhou, C. Shi, S. Long, Q. Yao, H. Ma, K. Chen, J. Du, W. Sun, J. Fan, B. Liu, et al., ACS Cent. Sci., 2023, 9, 1679–1691.

2 H. Yuan, B. Wang, F. Lv, L. Liu and S. Wang, Adv. Mater., 2014, 26, 6978–6982.

3 H. T. Feng, Y. Li, X. Duan, X. Wang, C. Qi, J. W. Y. Lam, D. Ding and B. Z. Tang, J. Am. Chem. Soc., 2020, 142, 15966–15974.

4 J. Tian, B. Li, F. Zhang, Z. Yao, W. Song, Y. Tang, Y. Ping and B. Liu, Angew. Chem., Int. Ed., 2023, 62, e202307288.

5 Z. Gao, S. Jia, H. Ou, Y. Hong, K. Shan, X. Kong, Z. Wang, G. Feng and D. Ding, Angew. Chem., Int. Ed., 2022, 61, e202209793.

6 W. Chen, Z. Wang, M. Tian, G. Hong, Y. Wu, M. Sui, M. Chen, J. An, F. Song and X. Peng, J. Am. Chem. Soc., 2023, 145, 8130–8140.

7 Q. T. Le, E. Chen, A. Salim, H. Cao, C. S. Kong, R. Whyte, J. Donington, W. Cannon, H. Wakelee, R. Tibshirani, et al., Clin. Cancer Res., 2006, 12, 1507–1514.

8 K. X. Teng, W. K. Chen, L. Y. Niu, W. H. Fang, G. Cui and Q. Z. Yang, Angew. Chem., Int. Ed., 2021, 60, 19912–19920.

9 M. Li, J. Xia, R. Tian, J. Wang, J. Fan, J. Du, S. Long, X. Song, J. W. Foley and X. Peng, J. Am. Chem. Soc., 2018, 140, 14851–14859.

10 Z. Zhou, J. Song, L. Nie and X. Chen, Chem. Soc. Rev., 2016, 45, 6597–6626.

11 W. Fan, P. Huang and X. Chen, Chem. Soc. Rev., 2016, 45, 6488–6519.

12 X. Wang, W. Sun, H. Shi, H. Ma, G. Niu, Y. Li, J. Zhi, X. Yao, Z. Song, L. Chen, et al., Nat. Commun., 2022, 13, 5091.

13 J. W. Yuan, Q. C. Peng, J. C. Fu, Q. Yang, Z. Y. Gao, Z. Y. Wang, K. Li, S. Q. Zang and B. Z. Tang, J. Am. Chem. Soc., 2023, 145, 27095–27102.

14 H. Wu, L. Wang, Y. Wang, Y. Shao, G. Li, K. Shao and E. U. Akkaya, Angew. Chem., Int. Ed., 2022, 61, e202210249.

15 B.-R. Xie, C.-X. Li, Y. Yu, J.-Y. Zeng, M.-K. Zhang, X.-S. Wang, X. Zeng and X.-Z. Zhang, CCS Chem., 2021, 3, 1187–1202.

16 S. Kolemen, T. Ozdemir, D. Lee, G. M. Kim, T. Karatas, J. Yoon and E. U. Akkaya, Angew. Chem., Int. Ed., 2016, 55, 3606–3610.

17 L. Chen, K. Sun, D. Hu, X. Su, L. Guo, J. Yin, Y. Pei, Y. Fan, Q. Liu, M. Xu, et al., Angew. Chem., Int. Ed., 2023, 62, e202218670.

18 J. Zou, J. Zhu, Z. Yang, L. Li, W. Fan, L. He, W. Tang, L. Deng, J. Mu, Y. Ma, et al., Angew. Chem., Int. Ed., 2020, 59, 8833–8838.

19 Y. Zhu, M. Gao, M. Su, Y. Shen, K. Zhang, B. Yu and F. J. Xu, Angew. Chem., Int. Ed., 2023, 62, e202306803.

20 C. Szabo, Nat. Rev. Drug Discovery, 2007, 6, 917–935.

21 S. Garcia-Gallego and G. J. Bernardes, Angew. Chem., Int. Ed., 2014, 53, 9712–9721.

22 C. Szabo, Nat. Rev. Drug Discovery, 2016, 15, 185–203.

23 Z. Shen, S. Zheng, Y. Fang, G. Zhang, C. Zhu, S. Liu and J. Hu, Angew. Chem., Int. Ed., 2023, 62, e202219153.

24 M. Zhang, J. Cheng, Z. Shen, P. Lin, S. Ding and J. Hu, Angew. Chem., Int. Ed., 2023, 62, e202314563.

25 J. Tian, B. Li, C. Wu, Z. Li, H. Tang, W. Song, G. B. Qi, Y. Tang, Y. Ping and B. Liu, J. Am. Chem. Soc., 2024, 146, 16458–16468.

26 J. Hu, G. Liu, C. Wang, T. Liu, G. Zhang and S. Liu, Biomacromolecules, 2014, 15, 4293–4301.

27 M. Tantama, Y. P. Hung and G. Yellen, J. Am. Chem. Soc., 2011, 133, 10034–10037.

28 S. Chen, Y. Hong, Y. Liu, J. Liu, C. W. Leung, M. Li, R. T. Kwok, E. Zhao, J. W. Lam, Y. Yu, et al., J. Am. Chem. Soc., 2013, 135, 4926–4929.

29 P. Saftig and K. Sandhoff, Nature, 2013, 502, 312–313.

30 T. M. Tsubone, W. K. Martins, C. Pavani, H. C. Junqueira, R. Itri and M. S. Baptista, Sci. Rep., 2017, 7, 6734.

31 B. Zhitomirsky and Y. G. Assaraf, Drug Resistance Updates, 2016, 24, 23–33.

32 Q. Xiao, H. Lin, J. Wu, X. Pang, Q. Zhou, Y. Jiang, P. Wang, W. Leung, H. Lee, S. Jiang, et al., J. Med. Chem., 2020, 63, 4896–4907.

33 P. K. Selbo, A. Weyergang, A. Hogset, O. J. Norum, M. B. Berstad, M. Vikdal and K. Berg, J. Controlled Release, 2010, 148, 2–12.

34 O. J. Norum, P. K. Selbo, A. Weyergang, K. E. Giercksky and K. Berg, J. Photochem. Photobiol., B, 2009, 96, 83–92.

35 G. Liu, J. Hu, G. Zhang and S. Liu, Bioconjugate Chem., 2015, 26, 1328–1338.

36 H. Maeda, Bioconjugate Chem., 2010, 21, 797–802.

37 S. Lv, M. Sylvestre, A. N. Prossnitz, L. F. Yang and S. H. Pun, Chem. Rev., 2021, 121, 11653–11698.